The influence of periodic islands in the flow field on a scalar tracer in the presence of a steady source

M. R. Turner, J. Thuburn & A. D. Gilbert

Mathematics Research Institute,
School of Engineering, Computing and Mathematics,
University of Exeter,
Exeter EX4 4QF, U.K.

Abstract

In this paper we examine the influence of periodic islands within a time periodic chaotic flow on the evolution of a scalar tracer. The passive scalar tracer is injected into the flow field by means of a steady source term. We examine the distribution of the tracer once a periodic state is reached, in which the rate of injected scalar balances advection and the molecular diffusion κ. We study the two–dimensional velocity field $\mathbf{u}(x, y, t) = 2\cos^2(\omega t)(0, \sin x) + 2\sin^2(\omega t)(\sin y, 0)$. As ω is reduced from an $O(1)$ value the flow alternates through a sequence of states which are either globally chaotic, or contain islands embedded in a chaotic sea. The evolution of the scalar is examined numerically using a semi–Lagrangian advection scheme.

By time–averaging diagnostics measured from the scalar field we find that the time–averaged length of the scalar contours in the chaotic region grow like $\kappa^{-1/2}$ for small κ, for all values of ω, while the dependence of the time–averaged maximum scalar value, $\overline{C_{\max}}$, depends strongly on ω as κ varies. In the presence of islands $\overline{C_{\max}} \sim \kappa^{-\alpha}$ for some α between 0 and 1 and with κ small, and we demonstrate that there is a correlation between α and the area of the periodic islands, at least for large ω. The limit of small ω is studied by considering a flow field that switches from $\mathbf{u} = (0, 2\sin x)$ to $\mathbf{u} = (2\sin y, 0)$ at periodic intervals. The small κ limit for this flow is examined using the method of matched asymptotic expansions.

Finally the role of islands in the flow is investigated by considering the time–averaged effective diffusion of the scalar field. This diagnostic can distinguish between regions where the scalar is well mixed and regions where the scalar builds up.

1   Introduction

When a scalar tracer is injected into a fluid flow, the advection process can create fine scale structure in the tracer, which is subsequently destroyed by molecular diffusion. This advection–diffusion combination tends to homogenize the scalar and eventually the system evolves into a uniform steady state if there is no additional source of scalar. However if additional scalar is injected into the flow via a steady source term, then, for a time periodic flow in a periodic domain, the system evolves into a periodic state, where scalar diagnostics oscillate about some time–averaged value (Thiffeault *et al.*, 2004; Doering and Thiffeault, 2006). The efficiency of statistically stationary, homogeneous, isotropic flows (which include turbulence) to mix scalars was examined by Doering and Thiffeault (2006). They calculate an upper bound for the scalar concentration for various source terms; however the actual maximum concentrations are sensitive to the velocity field, and in particular the existence of periodic islands in the flow. Advection–diffusion problems with a source term are also important in the study of air pollution (Tirabassi, 1989); thus understanding how much pollutant builds up in stagnant regions, such as islands, is very important. This study is therefore motivated by trying to understand better how scalar builds up in the presence of these islands, including the dependence on the size of the islands.

In the current study we examine the periodic states of time periodic flows by considering a scalar tracer which is injected steadily into an unsteady, two–dimensional, periodic velocity field. We choose the velocity field

$$\mathbf{u}(x, y, t) = 2\cos^2(\omega t)(0, \sin x) + 2\sin^2(\omega t)(\sin y, 0), \qquad (1.1)$$

which, depending on the value of ω, is either globally chaotic or consists of periodic islands embedded in a chaotic sea. This flow, which is a modification of the time–periodic sine flow (TPSF), is chosen so we can investigate how the steady state is dependent on the islands. By varying the control parameter ω we can change the period of the flow and hence the size of the periodic islands, and for certain values of ω the islands disappear altogether. The evolution of scalar in this flow in the absence of a source term has been studied by Cerbelli *et al.* (2003) and Giona *et al.* (2004). It is well known that periodic islands inhibit mixing by trapping scalar within them (Wiggins and Ottino, 2004; Gleeson, 2005), but a thorough study investigating the quantity of scalar that builds up in islands in the presence of a source term has not been carried out to date. Gleeson (2005) studies the evolution of a strip of scalar placed inside a flow field for two initial conditions, one when the scalar crosses a periodic island, and one where it does not. The results show that the scalar initially within the island winds up and homogenizes, but stays within the island, while the other case shows that the scalar becomes well mixed in the surrounding

2

chaotic sea without being transported into the periodic island. In this example a mixing measure $m(t)$ is defined, which in a 'vortexlike mixing period' decays as $Pe^{-\alpha}$ where Pe is the Péclet number (proportional to the inverse of the molecular diffusion) and α is a real scaling exponent. However in the current study the presence of a steady source means that there will be a continuous injection of scalar both into the islands and the chaotic region. The work of Doering and Thiffeault (2006) confirms that there will be an upper bound on the scalar value in the islands, but we will show a correlation between the time–averaged maximum scalar value in the islands and their size, for varying κ.

By considering time averages over one period of the flow field, we produce scalar diagnostics that are steady and hence are easier to analyze. We shall consider the evolution of both the time–averaged maximum scalar value $\overline{C_{\max}}$ and the time–averaged contour length, as functions of the molecular diffusion κ. The case of a slowly varying velocity field (small ω) is examined analytically by studying the time–periodic sine flow (TPSF) which has a velocity field that instantaneously switches between $\mathbf{u} = (0, 2\sin x)$ and $\mathbf{u} = (2\sin y, 0)$ periodically with period $2t_{\mathrm{s}}$. By the use of matched asymptotic expansions we determine how $C_{\max}$, and subsequently $\overline{C_{\max}}$, vary with κ.

As well as these diagnostics another useful measure is the *effective diffusion* of the scalar field. Transforming the advection–diffusion equation using a quasi–Lagrangian coordinate system (Butchart and Remsberg, 1986) based on the area inside scalar concentration contours (Nakamura, 1996; Winters and D'Asaro, 1996), leads to a pure diffusion equation, where the diffusion coefficient is known as the effective diffusion. The effective diffusion is a useful diagnostic tool because it requires no prior knowledge of the velocity field, as it depends solely on the instantaneous distribution of the scalar field. This makes it a very attractive tool for studying mixing and transport properties of complicated systems such as the atmosphere (Haynes and Shuckburgh, 2000a,b). Systematic studies of this diagnostic tool have shown that areas of high effective diffusion correspond to areas of well mixed scalar and areas of low effective diffusion occur in regions of poorly mixed scalar, such as in periodic islands (Shuckburgh and Haynes, 2003; Turner *et al.*, 2008). For this reason we adopt the effective diffusion in this study to compare the relative sizes of the well mixed region of the time–averaged effective diffusion for a flow with periodic islands and one without islands.

The present paper is laid out as follows. In §2 we formulate the problem and discuss the numerical scheme used to calculate the scalar field. In §3 we examine the kinematic behaviour of the flow. A careful study determines the parameter values for which we have periodic islands embedded in a chaotic flow and for which values we apparently have a globally chaotic flow. Section 4 presents the results of the numerical simulations of the advection–diffusion

3

equation including effective diffusion calculations and an analytical result for the TPSF problem. Our concluding remarks and some discussion are given in §5.

2 Formulation and numerical scheme

In an incompressible fluid flow, the evolution of a scalar tracer that has concentration $c(\mathbf{x}, t)$ is governed by the advection–diffusion equation

$$\frac{\partial c}{\partial t} + \mathbf{u} \cdot \nabla c = \nabla \cdot (\kappa \nabla c) + S, \qquad (2.1)$$

where $\mathbf{u}$ is a prescribed incompressible velocity field, $\kappa(\mathbf{x}, t)$ is the molecular scalar diffusion and $S(\mathbf{x}, t)$ is a source term. The current work uses the two–dimensional flow field given by (1.1) where ω is a real frequency and x and y are Cartesian coordinates. For simplicity we also consider the case when $\kappa(\mathbf{x}, t)$ is constant and the source term $S(\mathbf{x}, t) = \cos x$ which is steady and has zero mean.

This study examines the long time behaviour of (2.1) where, due to the presence of the source, the behaviour of the scalar field eventually becomes periodic in time and, from a Lagrangian point of view, the source term balances molecular diffusion over one period.

Although small scales are generated in the scalar field, the specified velocity field is smooth and large scale. Consequently, the Lagrangian timescale of the scalar in this problem is much longer than the Eulerian timescale. The problem therefore lends itself to solution by a semi–Lagrangian method (e.g. Staniforth and Côté, 1991). We use cubic Lagrange interpolation for the scalar advection, with a Crank–Nicolson treatment of the diffusion term. This makes the scheme second–order accurate in time overall and allows much longer time steps Δt to be used, without losing accuracy or stability, than would be possible with the Eulerian scheme used by Turner *et al.* (2008). Thus, the computation time required to reach the periodic state is greatly reduced. Nevertheless, we still find ourselves restricted in our parameter search by the computational time required to complete the runs. This is discussed further in §4.

3 Kinematic properties of the flow

Before embarking on a full numerical simulation of (2.1), we consider the kinematic properties of the flow field (1.1) by examining Poincaré sections of its structure.

To calculate the Poincaré sections, we first write the flow field as a system of two first order differential equations

$$\frac{dx}{dt} = 2\sin^2(\omega t)\sin y, \qquad \frac{dy}{dt} = 2\cos^2(\omega t)\sin x. \qquad (3.1)$$

These equations are then integrated from the set of initial conditions $(x_0, 0)$ and (x_0, π) where

$$x_0 = -\pi + 2\pi(j-1)/(N-1) \qquad j = 1, 2, 3, ..., N,$$

and for each initial condition the position of the fluid particle is represented by a dot in real space after each period of the flow $T = \pi/\omega$. For the resulting Poincaré sections in figure 1, $N = 30$ and for $\omega \leq 0.5$ we integrated to $t = 400T$ and to $t = 200T$ otherwise.

For large frequencies the direction of the shear flow changes rapidly and the results show that the Poincaré section has a cellular structure with four periodic 'islands' centred at $(0, \pm\pi)$ and $(\pm\pi, 0)$. Between these islands is a thin band of chaos which increases in thickness as ω is reduced. This can be seen when moving from $\omega = 3.5$ in figure 1(f) to $\omega = 2$ in figure 1(e). As ω is decreased further the size of the islands is reduced also because the longer flow period means that fluid particles are stretched out much further and so any island regions are eventually stretched out and removed. At $\omega \approx 0.75$ the islands disappear completely and we apparently have a globally chaotic flow. A globally chaotic flow can be seen in figure 1(b) where $\omega = 0.5$. However when $\omega = 0.3$ we find that the globally chaotic flow changes to one with small islands around $(0, \pm\pi)$ and $(\pm\pi, 0)$. Further reducing ω (not shown here) shows that $\omega = 0.2$ is fully chaotic, but $\omega = 0.1$ again has small islands. This is a resonant effect similar to that seen in the Mathieu equation (Nayfeh and Mook, 1979). Thus it is not true to say that the flow has islands for $\omega \gtrsim 0.75$: and is globally chaotic for $\omega \lesssim 0.75$, instead we have to be careful that our choice of ω generates a window where the flow does not contain islands if we wish to examine a globally chaotic flow. When we inject scalar into a globally chaotic flow we expect the scalar field to be well mixed and the maximum value of scalar $C_{\max}$ to be less than a flow case where there are islands present, as scalar builds up in such islands.

We can examine for which values of ω we expect to see the resonant islands around the points $(\pm\pi, 0)$ and $(0, \pm\pi)$ by studying a local solution about $(\pi, 0)$. Thus inserting $x' = x - \pi$ and $y' = y$ into (3.1) and linearising leads to

$$\frac{dx'}{dt} = 2\sin^2(\omega t)y', \qquad \frac{dy'}{dt} = -2\cos^2(\omega t)x'. \qquad (3.2)$$

(The other three points lead to either the same system of equations, or one with the minus sign swapped over). We now solve this system by integrating
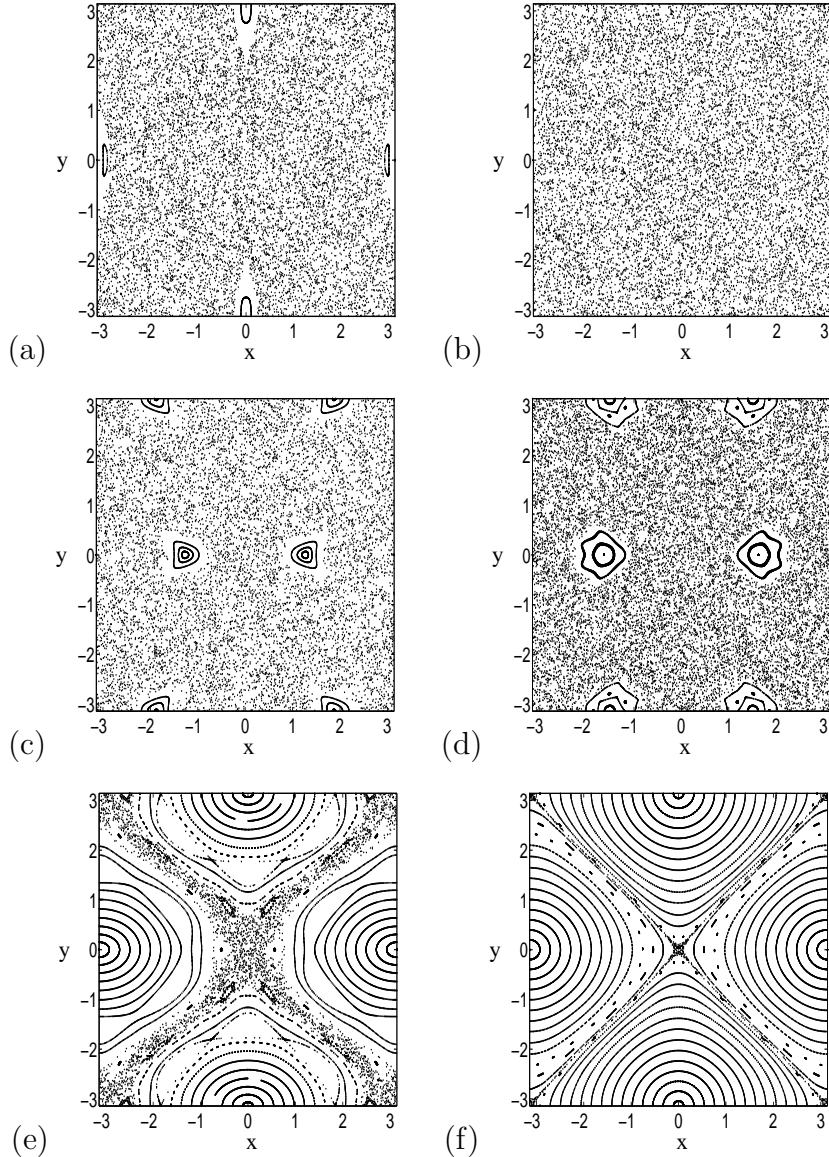
5

Fig. 1. Poincaré sections for the velocity field (1.1) for the cases (a) $\omega = 0.3$, (b) $\omega = 0.5$, (c) $\omega = 0.8$, (d) $\omega = 1$, (e) $\omega = 2$ and (f) $\omega = 3.5$.

using a fourth order Runge–Kutta scheme with the initial condition $x' = 10^{-3}$, $y' = 10^{-3}$. With these initial conditions we check the linear stability of (3.2) and we assume that linear stability implies islands in the Poincaré section and linear instability implies a globally chaotic flow. The results for the one parameter family ω are shown in figure 2(a), where the value 1 on the vertical axis represents chaos and 0 represents periodic orbits or islands. The results show that for $\omega \gtrsim 1.45$ there are always islands about this point as can be seen in figure 1(e) and (f). However as ω is reduced they disappear and then reappear at a more and more rapid rate when $\omega \lesssim 0.2$. The rate at which these islands appear and disappear can be seen in figure 2(b), which plots panel (a) as a function of $1/\omega$. Here we see a regular spacing of the windows
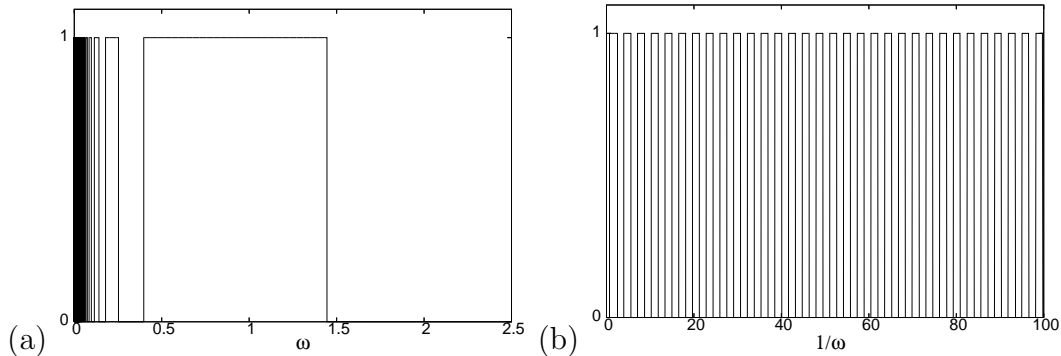
6

Fig. 2. Plot of (a) the parameter space for (3.2), where 0 on the vertical axis denotes periodic orbits and 1 denotes chaos. Panel (b) shows panel (a) plotted against $1/\omega$ to show an equal spacing of windows.

of ω values for which the islands are present. Note that for $\omega \gtrsim 0.75$ the flow can have islands at points corresponding to $(x, y) \neq (\pm\pi, 0)$ and $(0, \pm\pi)$ (cf figures 1(c) and 1(d)), whereas for $\omega < 0.75$ they only appear to occur at these four points. It is feasible that resonant islands could occur at points other than the four mentioned above, but our exploration of the $\omega-$space considered in this paper has not revealed any such points. Thus we assume that the four points considered here are the only such points.

Now that we know when and where the periodic islands appear in the flow field we can solve the advection–diffusion equation (2.1) and examine the evolution of the scalar field.

4   Numerical evolution of scalar field and steady state analysis

In this section we numerically study the solution of (2.1) in the large t limit where the scalar field has become periodic, due to the injection from the steady source. We demonstrate how the periodic scalar field and the length of various scalar contours vary over a period of the flow field, and we also show how $\overline{C_{\max}}$ varies with κ by time averaging the maximum value of the scalar field. This section ends with an analytical approach to solve the case where (1.1) has small ω. For this study we use the source distribution $S(x) = \cos x$. Initially we set the scalar concentration $c(x, y, t = 0) = 0$ and we let the system evolve with time, which gives a transient regime for early times where the scalar increases from $c = 0$ up to the steady state. The length of time of this transient phase depends on both ω and κ, and increases for small κ (inviscid flows) and large ω (short period flows). This limits the parameter range that we can study (mainly small κ and moderate κ with $\omega > 0.8$), but this does not appear to restrict any results in this paper.

7

To analyze the scalar field in the periodic state we use the diagnostics $C_{\max}(t)$ which is the maximum value of the scalar at any given time, and the length of the contour $c = C$, which we denote by L_C. Typically we consider the contour $C = 0$, as this contour always lies within the chaotic band regardless of the value of ω, hence these results should be consistent. However we do look at other scalar contour lengths later in this section.

In the periodic regime, the scalar field varies over the duration of a flow period $T = \pi/\omega$ and time averaging these diagnostics of this regime gives corresponding steady state quantities such as $\overline{C_{\max}}$ or $\overline{L_C}$. The variation of both $C_{\max}$ and L_0 for a selection of flow parameters is given in figure 3 as a function of t/T.
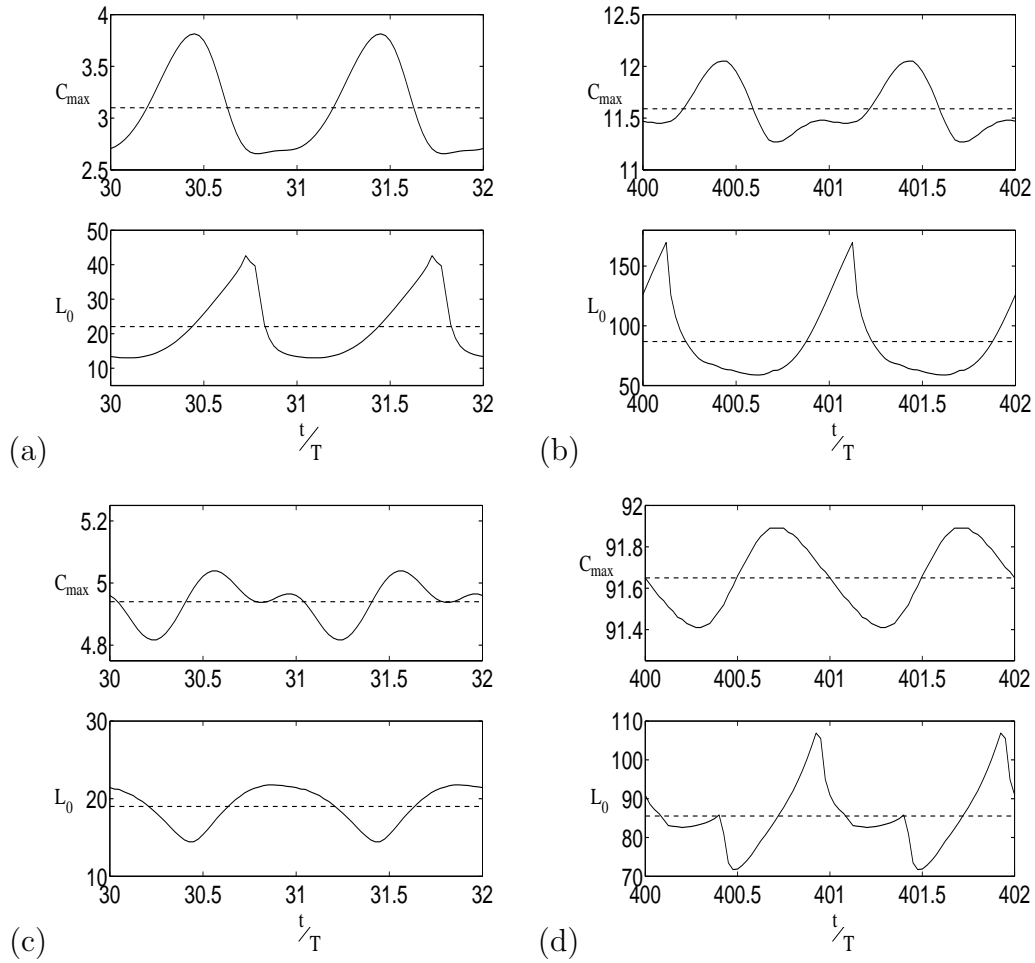

Fig. 3. Plot of both $C_{\max}$ and L_0 as a function of t/T for the cases (a) $(\omega, \kappa) = (0.5, 10^{-1})$, (b) $(\omega, \kappa) = (0.5, 10^{-3})$, (c) $(\omega, \kappa) = (1, 10^{-1})$ and (d) $(\omega, \kappa) = (1, 10^{-3})$. The dashed lines in each figure represent the equivalent value of $\overline{C_{\max}}$ or $\overline{L_0}$

Figure 3 graphs both $C_{\max}$ and L_0 for the parameter cases $(\omega, \kappa) = (0.5, 10^{-1})$, $(\omega, \kappa) = (0.5, 10^{-3})$, $(\omega, \kappa) = (1, 10^{-1})$ and $(\omega, \kappa) = (1, 10^{-3})$ in panels (a)

to (d) respectively. For each panel the respective time averaged value of the diagnostic is given by the horizontal dotted line. We note that at the beginning and end of each period, the flow stretches the scalar approximately parallel to the $y-$axis, which is aligned with the source term, and for the middle of the flow period it is being stretched approximately parallel to the $x-$axis which shears the scalar field and allows diffusion to act strongly on the fine scale structure. The first thing to note in figure 3 is that in the results with islands ($\omega = 1$) the variation of both $C_{\max}$ and L_0 is over a much smaller range of values. This is because the shear flow is changing direction much faster than in the $\omega = 0.5$ case, and so the islands rotate from being positioned over a negative part of the source to a position over a positive part or vice versa, thus not allowing large amounts of scalar to build up.

The general behaviour of the quantities in figure 3 is that both $C_{\max}$ and L_0 increase to some maximum value before rapidly decreasing to a minimum value after the flow field has rotated. Note that the rotation is not instantaneous and any increase or decrease in diagnostic values is also due to the smooth rotation of the flow field. However it appears that the actual timing of these maximum and minimum values is strongly linked to the values of κ and ω chosen. For example, for $(\omega, \kappa) = (0.5, 10^{-1})$ in panel (a) the maximum and minimum values of $C_{\max}$ occur around $t/T = 30.5$ and $t/T = 31$ respectively and for L_0 these are at $t/T = 30.75$ and $t/T = 31$ respectively. However as ω is increased to 1 in panel (c) the maximum and minimum values of $C_{\max}$ now occur at $t/T = 30.6$ and $t/T = 30.25$ and the L_0 extremes have swapped over to $t = 30T$ and $t = 30T + T/2$ respectively. Similar variations can be seen by considering the $\kappa = 10^{-3}$ cases. The time lag between the flow field changing and the scalar field changing is apparent in this figure, and will play a role later in determining how $\overline{C_{\max}}$ and $\overline{L_C}$ behave for varying ω and κ.

The results in figure 3 help us to understand how the scalar field behaves over the course of a time period of the flow. However to gain more insight we consider the real space images of the scalar field which are plotted in figure 4. This figure shows the four cases considered in figure 3 plotted at the midpoint of the period $t = nT + \frac{1}{2}T$ (left panels) and the end point $t = nT$ of the period (right panels), with red (mid grey) signifying large positive values and dark blue (dark grey) signifying large negative values of scalar. In each figure the zero contour L_0 is shown as the solid black line. For $\omega = 0.5$ there are no islands in the flow field; this gives a scalar field with regions of long stretched out regions of scalar. This is clearly seen for the $\kappa = 10^{-3}$ in panels (c) and (d). We can also clearly see that the zero contour is much longer in this case than the $\kappa = 10^{-1}$ case (panels (a) and (b)) due to its intricate form. As we increase ω to 1 (i.e shorten the flow period and introduce islands to the flow field) then we can see that the scalar field has a form which reflects the size of the islands. For $\kappa = 10^{-1}$ (panels (e) and (f)) four regions of scalar build up and are relatively obvious but they are much clearer in the $\kappa = 10^{-3}$ result in
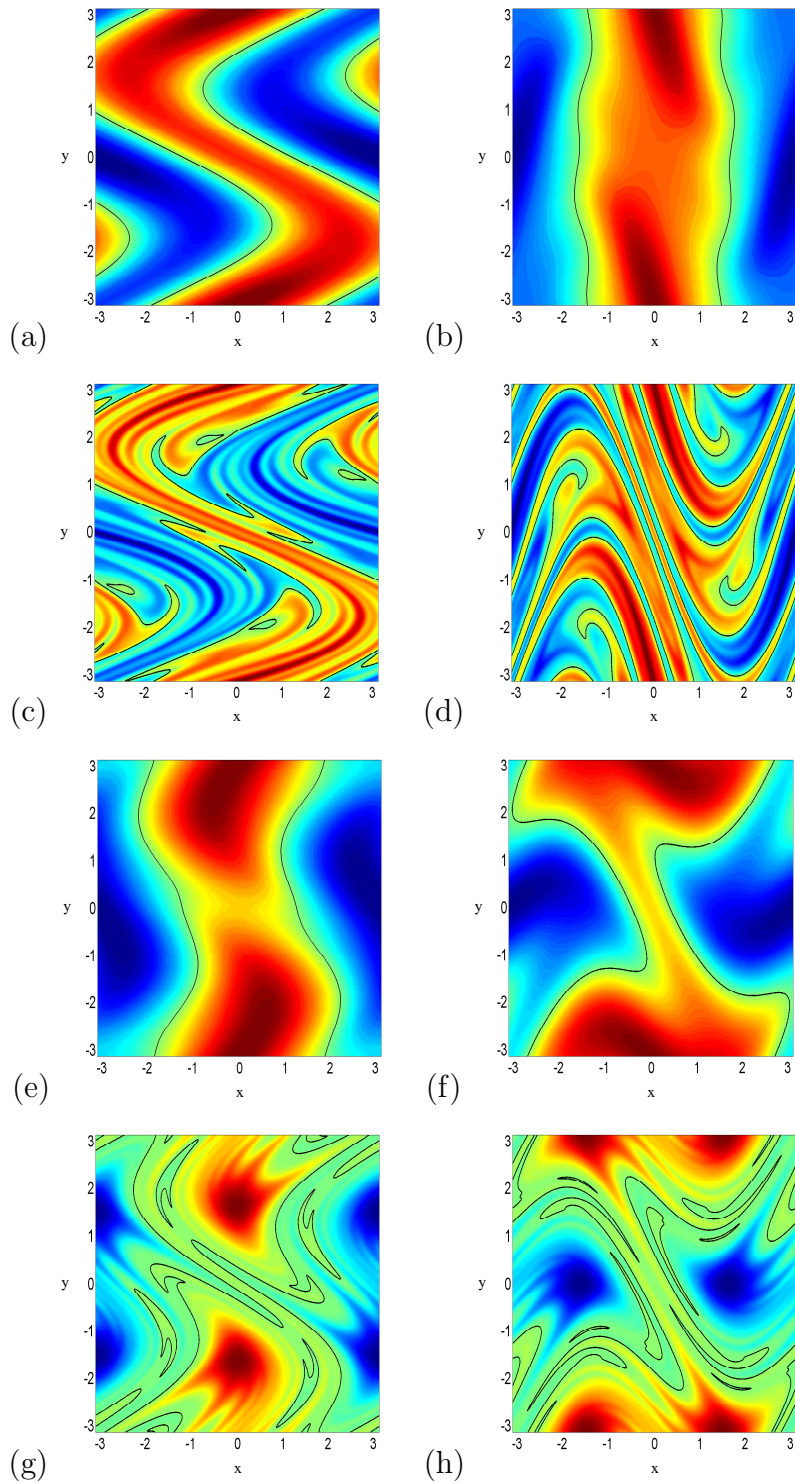
Fig. 4. Plots of the scalar field $c(x, y, t)$ in the periodically steady state at the midpoint of a period (left panels) and the end of a period (right panels) for (a,b) $(\omega, \kappa) = (0.5, 10^{-1})$, (c,d) $(\omega, \kappa) = (0.5, 10^{-3})$, (e,f) $(\omega, \kappa) = (1, 10^{-1})$ and (g,h) $(\omega, \kappa) = (1, 10^{-3})$. Red (mid grey) corresponds to large positive values of c and dark blue (dark grey) corresponds to large negative c. The black line is the contour $c = 0$.

panels (g) and (h) because the well mixed region of scalar is larger in this case and in this region the scalar homogenizes producing the green region (light grey) seen in the panels. In this case one can see that the zero contour has

pinched off into many smaller pieces, which allows diffusion to act and destroy these fine pieces, as seen in panels (g) and (h) in conjunction with figure 3(d). Figure 3(d) shows that L_0 decays from $t/T = 400$ before growing to a small peak around $t/T = 400.5$; there is then a rapid decay before rising sharply to the peak value just before $t/T = 401$. This is the shear flow breaking off the $C = 0$ contour into smaller pieces which are then stretched at first to give the increase in L_0. However they then become 'too' stretched and of a fine scale allowing diffusion to destroy these elements and giving the rapid drop in L_0.
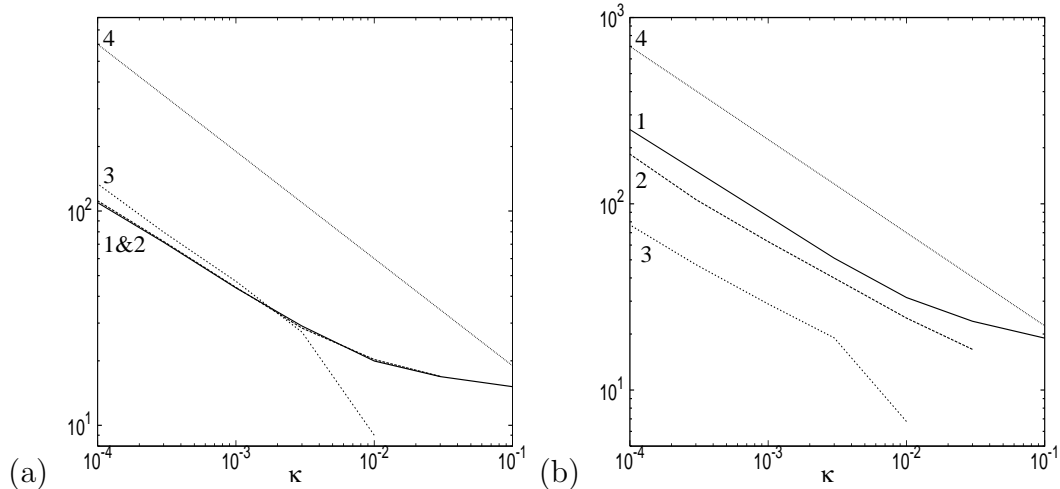

Fig. 5. Plot of $\overline{L_C}(\kappa)$ for (a) $\omega = 0.2$ and (b) $\omega = 1$ where the contours $C = 0$, 5 and 20 are labelled $1 - 3$ and line 4 is $\propto \kappa^{-1/2}$.

In figure 4 it is clear that as κ is reduced L_0 increases, but what is not so clear is how does the existence, or not, of islands affect the length of these contours and their dependence on κ? This question is addressed in figure 5 which plots the time–averaged contour length for $C = 0$, 5 and 20 for both $\omega = 0.2$ and 1 as a function of κ. For the flow with no islands ($\omega = 0.2$) in panel (a) we see that each of the three contour values has a length which grows almost as $\kappa^{-1/2}$, which is represented by line 4; this is commonly observed in chaotic flows (Thiffeault, 2006). The $C = 20$ contour line (line 3) grows most like $\kappa^{-1/2}$ while the $C = 0$ and 5 contour lines grow at a slightly slower rate. The $\overline{L_{20}}$ result initially grows at a different rate to the other two because when the $C = 20$ contour first exists for $\kappa = 10^{-2}$ this contour is in a region of low scalar stretching where the larger values of scalar are observed, and it is not until $\kappa = 0.003$, where $\overline{C_{\max}}$ has increased, that it is in a region of the flow where the contours grow more like $\kappa^{-1/2}$. A similar situation occurs for a flow with islands ($\omega = 1$) with the only apparent difference between this panel and that for $\omega = 0.2$ is now all three contours grow as $\kappa^{-1/2}$ for small κ. This shows that in a flow without islands, the time–averaged contour stretching is reduced in the middle of the chaotic band seen in figures 4(c) and 4(d). However this subtle change in growth rate is not expected to be important in determining how much scalar builds up in the islands, as many other factors are significant too.
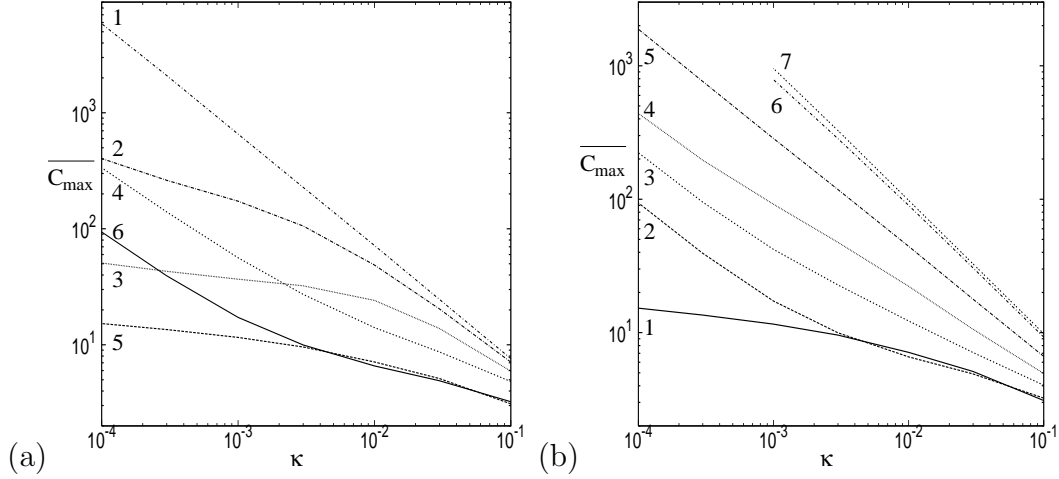
Fig. 6. Plot on a log–log scale of $\overline{C_{\max}}(\kappa)$ for (a) $\omega = 0.01$, 0.1, 0.2, 0.3, 0.5 and 0.8 labelled $1-6$ respectively, and (b) $\omega = 0.5$, 0.8, 0.9, 1.0, 1.2, 2.0 and 3.5 labelled $1-7$ respectively. Panel (a) is the corresponding small ω figure and panel (b) is the large ω figure, with the results $\omega = 0.5$ and 0.8 appearing on both for continuity.
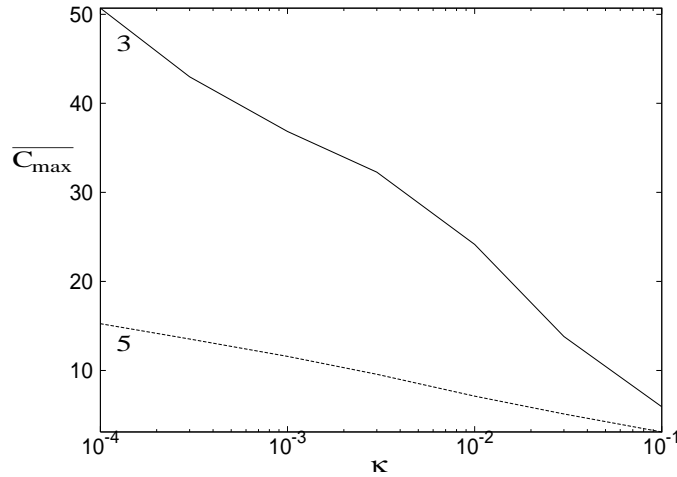

Fig. 7. Plot of $\overline{C_{\max}}(\kappa)$ on a log–linear plot for $\omega = 0.2$ and 0.5 marked as 3 and 5 respectively.

In figure 6 we plot $\overline{C_{\max}}(\kappa)$ for various values of ω on a log–log scale. In panel (a) we consider small values of $\omega = 0.01$, 0.1, 0.2, 0.3, 0.5 and 0.8 and these are labelled $1-6$ respectively, and in panel (b) we consider larger values of $\omega = 0.5$, 0.8, 0.9, 1.0, 1.2, 2.0 and 3.5 which are labelled $1-7$ respectively. The intermediate values of $\omega = 0.5$ and 0.8 are plotted on both panels to link the two together and give the reader a sense of the whole parameter range without a congested figure. For the small values of ω in panel (a) we see a typical behaviour emerging. When ω is moderately small and the flow field contains no islands, such as for lines 3 and 5, we see that $\overline{C_{\max}}$ does not grow as an inverse power of κ, and in fact when these two results are plotted on a log–linear plot in figure 7 they give approximate straight lines which suggests

12

a growth of $\overline{C_{\max}} \propto -\ln\kappa$. The reason for this growth dependence is not clear, and it is not true of all globally chaotic flows. We know this is the case because as we reduce ω further to 0.1 and 0.01, both of which have no resonance islands from §3, we find that $\overline{C_{\max}}$ begins to grow approximately as an inverse power of κ. (This can be seen by considering figure 2(b).) In fact the $\omega = 0.01$ result (line 1) can be shown to grow like κ^{-1} plus some smaller correction terms. This analysis is carried out in §4.1. For the cases in panel (a) where there are islands, $\omega = 0.3$ (line 4) and $\omega = 0.8$ (line 6), we see that for larger κ these results grow much like their non–island counterparts, down to some critical value of κ where the effect of the islands becomes significant, and then they begin to grow as $\kappa^{-\alpha}$ for some $\alpha \in (0,1]$.

In the corresponding large ω figure, figure 6(b), we observe that as ω increases, the value of the critical κ, where the role of the islands becomes significant, moves to larger κ values until by $\omega = 1$ (line 4), values of $\overline{C_{\max}}$ appear to grow $\propto \kappa^{-\alpha}$ over the whole range of κ considered. The corresponding value of α for this growth itself increases with ω until $\omega \approx 3.5$ (line 7) where it has the approximate value 1. This is because the scalar builds up in the islands and gives a scalar distribution of $c(x,y) \approx 1/(2\kappa)(\cos x - \cos y)$ as noted in Turner *et al.* (2008). The results of $\omega = 2.0$ and 3.5 (lines 6 and 7) are not computed all the way down to $\kappa = 10^{-4}$ as the other results are, because as ω becomes larger the number of flow periods that have to be completed before a steady state is achieved increases greatly; however results down to this value of κ are not required to get a clear picture of how the scalar behaves for these values of ω. One question still remains: can we link the value of the exponent α to the size of the periodic islands?
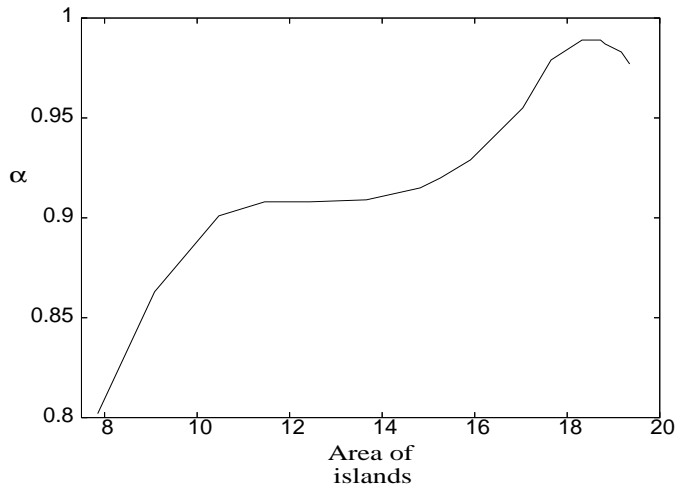

Fig. 8. Plot of the scaling exponent of $\overline{C_{\max}}$, α, as a function of the area of the periodic islands in the flow field.

In figure 8 we plot the scaling exponent of $\overline{C_{\max}}$, α, as a function of the area of the periodic islands in the flow field. For ω values between 1.2 and 3.5, we calculate the area of the islands by integrating (3.1) from a regularly spaced

array of positions in the domain $x \in [0, \pi]$, $y \in [0, \pi]$ and observing whether or not the particle path completes a periodic cycle, i.e. it comes back to its starting position. The area of the islands is then calculated as the fraction of periodic orbits compared to the chaotic orbits scaled up to the whole $[-\pi, \pi]^2$ domain. The corresponding value of α on the other hand is calculated by taking the gradient between the values $\kappa = 10^{-3}$ and 3×10^{-3} in figure 6(b). Both these calculations are prone to numerical error; however test calculations have shown that the maximum error for both values is around 3%. Thus figure 8 shows that by investigating this region of parameter space we find a correlation between the size of the islands and the scaling exponent α. It is not clear if the correlation could be made linear by plotting α against another measure of the islands such as their circumference, because although the islands are clearly defined in the flow field they are surrounded by regions of weak stretching which could also be significant to the build up of scalar within the islands. Thus the calculation of a circumference is difficult. Also if we consider figures 1(d) and 4(h), we see that the region of scalar build up in figure 4(h) is larger than the physical islands in figure 1(d). The scalar field also has fingers of scalar being stretched out which may also be significant in the calculation of α. If this investigation were continued to smaller island areas then we may also find another branch of solutions appearing in figure 8. If this were to happen it would show that α does not corrolate exactly with the area of the islands, but it could help to understand how α scales.

From figure 6(b) we see that $\overline{C_{\max}}$ grows like $\kappa^{-\alpha}$ in the large ω limit and moreover that there is a correlation between α and the size of the flow islands. However the exact scaling exponent for small ω is less clear, and this limit is examined further in the next section by considering a simplified model of the flow field.

4.1   Understanding the small ω limit: Analysis of the TPSF

To understand the scalar distribution in the small ω limit of the shear flow (1.1), we simplify the problem to one that can be analyzed more easily. We consider the flow consisting of two shearing motions where we 'switch' from one to the other after a given time t_{s}; this is known in the literature as the time–periodic sine flow (TPSF) (Cerbelli et $al.$, 2003; Giona et $al.$, 2004). Thus for one period our flow becomes

$$\mathbf{u} = \begin{cases} 2\sin x\, \hat{\mathbf{y}} & 0 < t \leq t_{\mathrm{s}}, \\ 2\sin y\, \hat{\mathbf{x}} & t_{\mathrm{s}} < t \leq 2t_{\mathrm{s}}. \end{cases}$$

This simplified flow takes away the complication of the flow axis varying between these two shear flows as in (1.1). The analysis in this section shows

that the solution for the scalar field in the initial half of the period is easy to examine analytically, while the second half leads to a boundary layer type problem for small κ. Before carrying out an analytical study we first examine the numerical results.
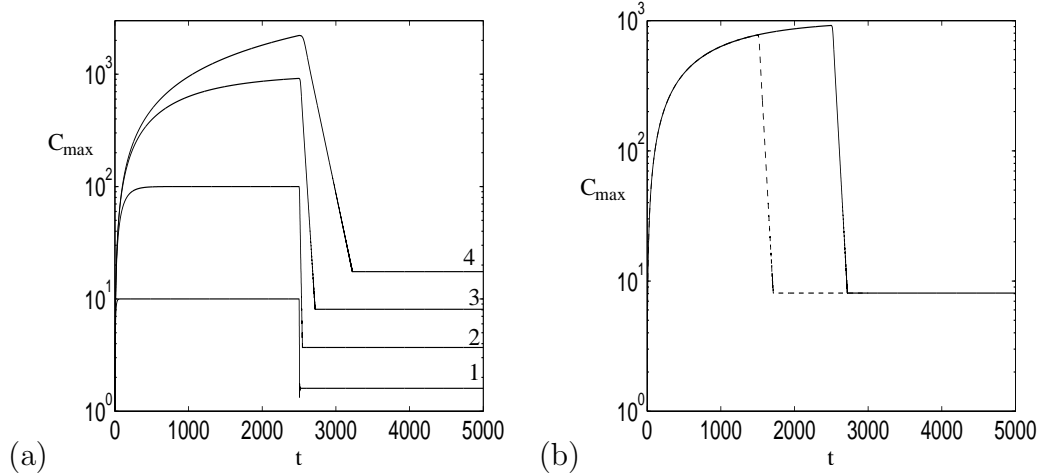

Fig. 9. Plot of $C_{\max}(t)$ for the TPSF. Panel (a) plots this quantity for $\kappa = 10^{-1}$, 10^{-2}, 10^{-3} and 10^{-4} labelled $1 - 4$ respectively, where $t_{\mathrm{s}} = 2500$. Panel (b) shows the case $\kappa = 10^{-3}$ but with $t_{\mathrm{s}} = 2500$ (solid line) and $t_{\mathrm{s}} = 1500$ (dotted line).

Figure 9(a) plots $C_{\max}(t)$ for the TPSF with $t_{\mathrm{s}} = 2500$ for $\kappa = 10^{-1}$, 10^{-2}, 10^{-3} and 10^{-4} labelled $1 - 4$ respectively. We observe that over the first half of the period, $C_{\max}$ increases to κ^{-1}, if t_{s} is large enough to allow this. This happens because for this time the shear flow acts parallel to the injection of scalar from the source and scalar builds up over this half period until it balances diffusion and $c(x, y) = \kappa^{-1} \cos x$. However for $t_{\mathrm{s}} < t < 2t_{\mathrm{s}}$ the shear flow acts perpendicular to the source, effectively stretching out the scalar into very fine filaments, which diffusion can then act on and remove. Thus at some point $C_{\max}$ reaches a constant value, a steady state; however for smaller values of κ the diffusion is weaker and it takes longer for the tracer to cascade to the scales at which diffusion balances stretching. Figure 9(b) again plots $C_{\max}$ in this TPSF for $\kappa = 10^{-3}$, but with two values of t_{s}. The outcome is that the steady state for $t_{\mathrm{s}} < t < 2t_{\mathrm{s}}$ is independent of the form of c at $t = t_{\mathrm{s}}$, hence we can analyze this part of the period by considering the steady form of (2.1) for simplicity.

By examining the real space plot of the scalar field $c(x, y)$ in the steady state for $t_{\mathrm{s}} < t < 2t_{\mathrm{s}}$ in figure 10, we can clearly see that as κ is reduced (see panel (b) for $\kappa = 10^{-3}$) the scalar distribution becomes concentrated around $y = 0$ and $\pm \pi$. This is not as clear for larger values of κ, such as $\kappa = 10^{-1}$ in panel (a), and so to understand how $C_{\max}$ varies with κ we investigate the limit of small κ.
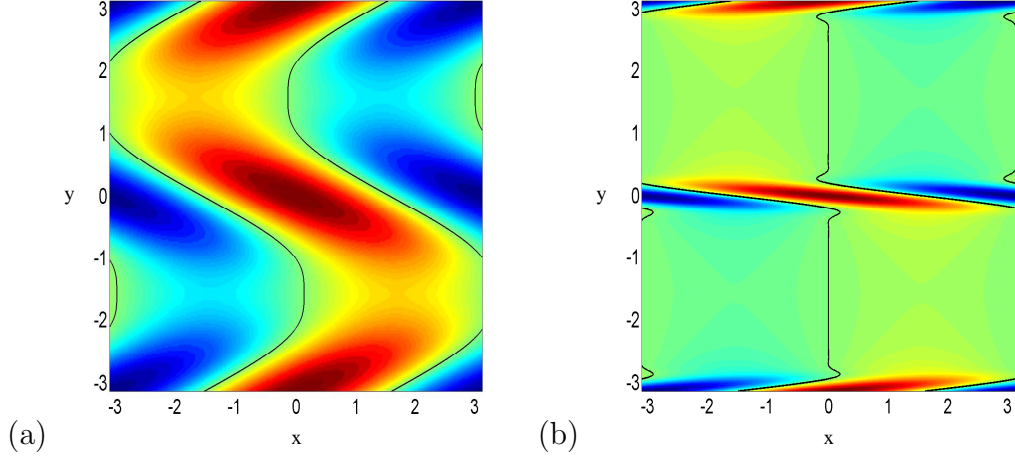
15

Fig. 10. Plot of the scalar field for the TPSF for $t_s < t < 2t_s$ and for (a) $\kappa = 10^{-1}$ and (b) $\kappa = 10^{-3}$. Red (mid grey) corresponds to large positive values of c and dark blue (dark grey) corresponds to large negative c. The black line is the contour $c = 0$.

4.1.1 Steady solution for $t \le t_s$

For the first half of the flow period, the steady form of (2.1) simplifies to

$$2\sin x\,\frac{\partial c}{\partial x} = \kappa\nabla^2 c + \cos x. \tag{4.1}$$

This equation can easily be solved by seeking a solution for $c(x,y)$ in terms of its Fourier components

$$c = c_{1,0}e^{ix} + c_{1,1}e^{i(x+y)} + c_{1,-1}e^{i(x-y)} + c_{0,1}e^{iy} + ... + \text{c.c.},$$

and then equating the coefficients of each component. Doing this we find that $c_{1,0} = 1/(2\kappa)$ and all other coefficients are zero. Thus

$$c = \frac{e^{ix}}{2\kappa} + \text{c.c.} = \frac{\cos x}{\kappa},$$

and hence $C_{\max} = \kappa^{-1}$ for large times, as observed in figure 9(a).

4.1.2 Steady solution for $t_s < t < 2t_s$

For the second half of the flow period the steady form of (2.1) takes the similar form

$$2\sin y\,\frac{\partial c}{\partial x} = \kappa\nabla^2 c + \cos x. \tag{4.2}$$

In this case, as the flow is independent of x we can assume that the scalar is harmonic in x with wavenumber 1. Thus for small κ we are seeking a solution

16

to (4.1) in the form

$$c = \left(c_0(y,t) + \kappa c_1(y,t) + O(\kappa^2)\right) e^{ix} + \text{c.c.}, \tag{4.3}$$

where we denote $\tilde{c} = c_0(y,t) + \kappa c_1(y,t) + O(\kappa^2)$. Substituting this into (4.1) gives at $O(1)$,

$$2ic_0 \sin y = \frac{1}{2}, \tag{4.4}$$

and at $O(\kappa)$

$$2ic_1 \sin y = \left(\frac{\partial^2}{\partial y^2} - 1\right) c_0. \tag{4.5}$$

Solving these two algebraic equations for c_0 and c_1 gives

$$c = \left(-\frac{i}{4\sin y} - \frac{\kappa \cos^2 y}{2\sin^4 y}\right) e^{ix} + \text{c.c.} \,.$$

However this expression has a singularity as $y \to 0$; in fact in this limit the above expression becomes

$$c = \left(-\frac{i}{4y} - \frac{\kappa}{2y^4}\right) e^{ix} + \text{c.c.}, \tag{4.6}$$

which contradicts figure 9 that shows a finite value of $C_{\max}$ at $y = 0$. Thus using this knowledge, and figure 10(b), we know that there is a layer about $y = 0$ (or similarly $y = \pm\pi$) where the diffusive effects are more important.

Substituting (4.3) into (4.2) and expanding about $y = 0$ leads to the equation

$$\frac{\partial^2 \tilde{c}}{\partial y^2} - \left(\frac{2iy}{\kappa} + \kappa\right)\tilde{c} = -\frac{1}{2\kappa}.$$

We solve this problem by calculating the Green's function $G(y,s)$ which satisfies

$$\frac{\partial^2 G}{\partial y^2} - \left(\frac{2iy}{\kappa} + \kappa\right) G = \delta(y - s), \tag{4.7}$$

where $\delta(X)$ is the Dirac delta function. The Green's function must also satisfy the jump conditions

$$[G]_{y=s^-}^{y=s^+} = 0, \quad \text{and} \quad \left[\frac{\partial G}{\partial y}\right]_{y=s^-}^{y=s^+} = 1.$$

The Green's function is calculated by transforming the homogeneous form of (4.7) in the Airy equation

$$\frac{\partial^2 G}{\partial Y^2} - YG = 0, \tag{4.8}$$

17

by changing variables to $Y = Ay$ where $A^3 = 2i/\kappa$, and neglecting the small κ term in the brackets. To have exponential decay for large Y we choose the solution

$$G(Y, s) = \alpha(s)\text{Ai}(Y).$$

We convert this expression back into $y-$space and we take $A = (2/\kappa)^{1/3}e^{i\pi/6}$ for $s < y$ and $A = (2/\kappa)^{1/3}e^{5i\pi/6}$ for $y < s$. (The third root gives y purely imaginary and is of no significance for this problem). This gives the Green's function as

$$G = \begin{cases} \alpha(s)\text{Ai}(fy) & s < y, \\ \beta(s)\text{Ai}(e^{2\pi i/3}fy) & y < s, \end{cases} \tag{4.9}$$

where $f = (2/\kappa)^{1/3}e^{i\pi/6}$ and $\alpha(s)$ and $\beta(s)$ are arbitrary functions. Solving for $\alpha(s)$ and $\beta(s)$ using the jump conditions gives

$$G = \begin{cases} -2\pi e^{i\pi/6}f^{-1}\text{Ai}(e^{2\pi i/3}fs)\text{Ai}(fy) & s < y, \\ -2\pi e^{i\pi/6}f^{-1}\text{Ai}(fs)\text{Ai}(e^{2\pi i/3}fy) & y < s. \end{cases} \tag{4.10}$$

Thus the general solution for $\tilde{c}(y)$ is

$$\tilde{c}(y) = -\int_{-\infty}^{\infty} \frac{G(s, y)}{2\kappa} \, ds,$$

which when integrated gives

$$\tilde{c} = \frac{\pi}{(2\kappa^2)^{1/3}} \left(\frac{e^{i\pi/6}\kappa^{1/3}}{3 \cdot 2^{1/3}}\text{Ai}(fy) + \text{Ai}(fy)\int_0^y \text{Ai}(e^{2\pi i/3}fs)ds + \text{Ai}(e^{2\pi i/3}fy)\int_y^\infty \text{Ai}(fs)ds \right). \tag{4.11}$$

By using the asymptotic expressions from pages 448 and 449 of Abramowitz and Stegun (1964) the leading order term of the large y expansion of (4.11) is

$$\tilde{c} \sim -\frac{i}{4y},$$

which agrees with (4.6). Also from the numerical simulations in this section we know that the maximum value of c occurs at $y = 0$, so evaluating (4.11) at $y = 0$ gives

$$c = 2\tilde{c}\cos x, \quad \tilde{c} = \frac{\pi\text{Ai}(0)}{3^{1/2}2^{2/3}\kappa^{1/3}},$$

and

$$C_{\text{max}} \sim 0.811\kappa^{-1/3}. \tag{4.12}$$

This asymptotic value of C_{max} (dashed line) is plotted with the value obtained from the full numerical simulation (solid line) in figure 11. Note that the agreement is excellent for small κ.
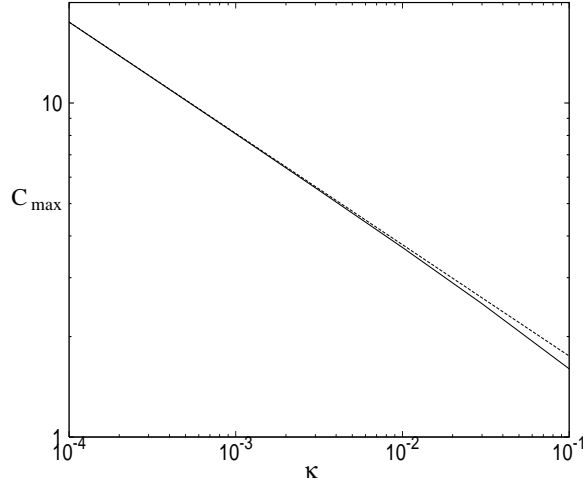
18

Fig. 11. Plot of $C_{\max}(\kappa)$ for the TPSF ($t_{\mathrm{s}} < t < 2t_{\mathrm{s}}$), with the simulation results as the solid line and the asymptotic result (4.12) as the dashed line.

Linking this result back to the $\omega = 0.01$ result (line 1) of figure 6(a) shows that as $\omega \to 0$ then $\overline{C_{\max}} \sim \frac{1}{2}(\kappa^{-1} + 0.811\kappa^{-1/3} + o(\kappa^{-1/3}))$, which when compared to the $\omega = 0.01$ result shows reasonable agreement. The agreement would improve as ω is reduced further, but gaining this result numerically is beyond the parameter range that we can easily compute.

4.2 Effective diffusion

A useful diagnostic for examining scalar fields is the effective diffusion of the scalar field (Nakamura, 1996; Winters and D'Asaro, 1996; Shuckburgh and Haynes, 2003; Turner *et al.*, 2008). This diagnostic has the useful property that it is large in regions where the scalar field is well mixed, and low in regions of poorly mixed scalar (Nakamura (1996); Shuckburgh and Haynes (2003)), thus in this section we shall apply it to scalar fields from flows with and without islands to try to understand how the scalar mixes in these flows.

The time evolution of the scalar in the transformed isotracer coordinates is determined as a function of area in two dimensions (Nakamura, 1996) or volume in three dimensions (Winters and D'Asaro, 1996). For the two–dimensional case we define the area of a contour C as the region bounded by this contour, i.e. everywhere where $c(\mathbf{x}, t) \leq C$. Thus we write

$$A = \int \int H(C - c(\mathbf{x}, t)) \, dA, \qquad (4.13)$$

where $H(X)$ is the Heaviside function. Under this change of coordinates (2.1)

19

becomes

$$\frac{\partial C}{\partial t} = \frac{\partial}{\partial A}\left(K_{\text{eff}}(A,t)\frac{\partial C}{\partial A}\right) + \langle S\rangle_A, \qquad (4.14)$$

where the effective diffusion can be written as

$$K_{\text{eff}} = \frac{\partial A}{\partial C}\int_{\gamma(C,t)}\kappa|\nabla c|\,ds = \frac{\langle\kappa|\nabla c|^2\rangle_A}{(\partial C/\partial A)^2}. \qquad (4.15)$$

The contour $\gamma(C,t)$ bounds the region A at a time t, and the weighted contour average of a quantity χ is given by

$$\langle\chi\rangle_A = \frac{\partial}{\partial A}\int_{c\leq C(A,t)}\chi\,dA = \left(\int_\gamma\frac{ds}{|\nabla c|}\right)^{-1}\int_\gamma\chi\frac{ds}{|\nabla c|}.$$

In this study we calculate the effective diffusion of a particular scalar contour C using both forms of (4.15) and this then acts as a check on the resolution of our code. For more information on the numerical evaluation of the second method in (4.15) see Shuckburgh and Haynes (2003) or Turner *et al.* (2008).

In this section we consider the time–averaged form of K_{eff} to give a view of how the scalar is mixed over one period of the flow. Thus we define the time–averaged effective diffusion as

$$\widehat{K}_{\text{eff}} = \overline{K_{\text{eff}}\frac{\partial C}{\partial A}}\bigg/\overline{\frac{\partial C}{\partial A}}. \qquad (4.16)$$

Previous studies have shown that areas of large effective diffusion correspond to regions of the flow where the scalar is well mixed (Nakamura, 1996; Shuckburgh and Haynes, 2003; Turner *et al.*, 2008). Thus we consider how the time–averaged effective diffusion may look for two flow fields, one with islands ($\omega = 1$) and one without ($\omega = 0.5$). These effective diffusions $\widehat{K}_{\text{eff}}$ are plotted for $\omega = 0.5$ in figure 12(a) and $\omega = 1$ for figure 12(b) both for $\kappa = 10^{-1}$, 10^{-2}, 10^{-3} and 10^{-4} labelled 1 to 4 respectively. In figure 12 we plot $\widehat{K}_{\text{eff}}$ as a function of A, thus $A = 0$ corresponds to $C = -C_{\max}$, $A = 4\pi^2$ corresponds to $C = C_{\max}$ and $A = 2\pi^2$ at $C = 0$.

One clear distinction to note from the two panels in figure 12 is that $\widehat{K}_{\text{eff}}(A)$ for $\omega = 0.5$ has a much wider profile than for $\omega = 1$, i.e. that $\widehat{K}_{\text{eff}} > 1/2\max(\widehat{K}_{\text{eff}})$ over a much larger range of area values for $\omega = 0.5$. For $\kappa > 10^{-2}$, $\widehat{K}_{\text{eff}}$ is larger for most values of A for $\omega = 0.5$, showing that a globally chaotic flow mixes scalar better than a flow with islands ($\omega = 1$). However as κ is reduced to 10^{-4} (line 4 in figure 12) we see that although $\widehat{K}_{\text{eff}}$ has a larger value (suggesting that the scalar is generally better mixed) over most of the domain for $\omega = 0.5$, there is a region around $A = 2\pi^2$ for $\omega = 1$ where $\widehat{K}_{\text{eff}}$ is larger, suggesting that the chaotic band seen in figures 4(g) and 4(h) contains scalar which is
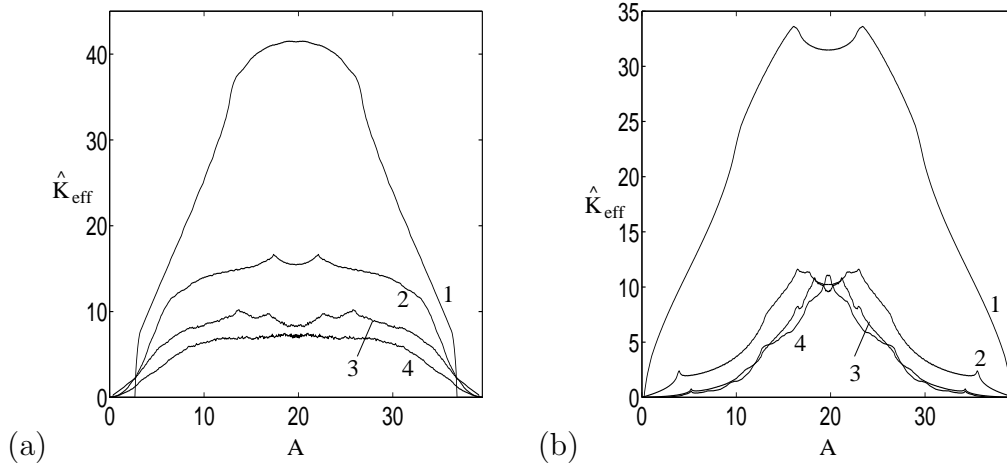
20

Fig. 12. Plot of the time–averaged effective diffusion $\widehat{K}_{\text{eff}}(A)$ for (a) $\omega = 0.5$ and (b) $\omega = 1$ with curves for $\kappa = 10^{-1}$, 10^{-2}, 10^{-3} and 10^{-4} labelled 1 to 4 respectively.

better mixed than the scalar seen in figures 4(c) and 4(d). Another point to note is that for $\omega = 0.5$, there is a clear difference between the $\kappa = 10^{-3}$ (line 3) and the $\kappa = 10^{-4}$ (line 4) results, while for $\omega = 1$ these two results are much more similar. This suggests that if $\widehat{K}_{\text{eff}}$ has an inviscid limit ($\kappa \to 0$) then the presence of islands may cause this limit to be obtained for a larger value of κ.

Turner *et al.* (2008) calculate results for $\widehat{K}_{\text{eff}}$ for $\kappa = 10^{-2}$, 10^{-3} and 10^{-4} using an Eulerian code. The restrictions using this code mean that steady states were hard to reach as they require very long time integrations, and in fact the results for $\kappa = 10^{-3}$ and 10^{-4} (along with 10^{-5} and 10^{-6}) in figure 13 of Turner *et al.* (2008) are not at a steady state, as speculated in the previous paper. However the semi–Lagrangian code in the current paper allows us to integrate for long time periods, so we can be sure that the results in figure 12(b) really are steady. Thus for these steady results we note that $\widehat{K}_{\text{eff}}$ for 10^{-3} and 10^{-4} are fairly similar; however we would still need to examine much smaller values of κ to fully determine whether or not an inviscid limit for $\widehat{K}_{\text{eff}}$ actually exists, and this question is left for future research.

5 Conclusions and discussion

In this paper we studied the behaviour of a scalar field in a velocity field with a steady source of scalar. The velocity field takes the form of a shear flow which changes from being approximately parallel to the y−axis to being approximately parallel to the x−axis periodically with period $T = \pi/\omega$. The parameter ω can be varied and the flow field changes from configurations where the Poincaré section is globally chaotic to situations where it has islands

21

surrounded by a chaotic sea. As ω is decreased the globally chaotic and island cases alternate at the rate $1/\omega$ due to a resonance effect of the flow field. Throughout this work we have concentrated on the large time form of the scalar when it is in a periodic state and we can sensibly define a time average for the scalar diagnostics over each period of the flow.

The results show that the time–averaged lengths of scalar contours in the chaotic region approximately increase as $\kappa^{-1/2}$ for both flows with islands and without; however the time–averaged maximum value of the scalar, $\overline{C_{\max}}$, depends more strongly on the size of the flow islands with larger islands giving a larger value of $\overline{C_{\max}}$. The flow field in (1.1) is not typical of an atmospheric flow, however this result is still of interest to those investigating the build up of pollutants in the atmosphere or other fluid flows. For large values of ω, the scalar field and flow field has an almost cellular structure, and $\overline{C_{\max}} \sim \kappa^{-1}$, while as ω is decreased $\overline{C_{\max}} \sim \kappa^{-\alpha}$ where α decreases from 1 and there is a correlation between α and the area of the flow islands. This algebraic growth, as opposed to the $-\ln\kappa$ type growth seen in the simulations, also begins to occur for smaller values of κ as ω is reduced. At $\omega \approx 0.75$ the periodic islands disappear and at this point $\overline{C_{\max}}$ appears to increase like $-\ln\kappa$. Thus the presence of the islands in the flow affects the scalar field by inhibiting mixing and allowing scalar concentrations to build up.

For small values of ω where the flow field exhibits a resonance effect, $\overline{C_{\max}}$ again appears to grow like $\kappa^{-\alpha}$ for an exponent $\alpha \in (0,1)$, but on careful examination it actually grows as $\kappa^{-\alpha}$ plus a small correction term. For the case of very small ω we calculate this correction term by considering the time–periodic sine flow which acts parallel to the $y-$axis for a fixed amount of time before switching to acting parallel to the $x-$axis. In this flow field the scalar builds up over the first period of the flow and then is sheared perpendicular to the source for the second half of the period. For this flow the scalar rose to the constant value $C_{\max} = \kappa^{-1}$ over the first half the period and then reduced to another constant value for the second half of the flow. In this half, for small κ, the scalar becomes concentrated at $y = 0$ in a thin boundary layer, and the solution to this problem is found using matched asymptotic expansions to be $C_{\max} = 0.811\kappa^{-1/3}$. This means that as $\omega \to 0$, $\overline{C_{\max}} \to \frac{1}{2}(\kappa^{-1} + 0.811\kappa^{-1/3})$.

Acknowledgments

References

Abramowitz, M. and Stegun, I. A. (1964). *Handbook of Mathematical Functions*. Dover.

Butchart, N. and Remsberg, E. E. (1986). Area of the stratospheric polar vortex as a diagnostic for tracer transport on an isentropic surface. *J. Atmos. Sci.*, **43**, 1319–1339.

Cerbelli, S., Adrover, A., and Giona, M. (2003). Enhanced diffusion regimes in bounded chaotic flows. *Phys. Lett. A*, **312**(5-6), 355–362.

Doering, C. R. and Thiffeault, J.-L. (2006). Multiscale mixing efficiencies for steady sources. *Phys. Rev E*, **74**, 025301–1–4.

Giona, M., Adrover, A., Cerbelli, S., and Vitacolonna, V. (2004). Spectral properties and transport mechanisms of partially chaotic bounded flows in the presence of diffusion. *Phys. Rev. Lett.*, **92**(11), 114101–1–4.

Gleeson, J. P. (2005). Transient micromixing: examples of laminar and chaotic stirring. *Phys. Fluids*, **17**(10), 100614, 9.

Haynes, P. and Shuckburgh, E. (2000a). Effective diffusion as a diagnostic of atmospheric transport, 1. stratosphere. *J. Geophys. Res*, **105**, 22777–22794.

Haynes, P. and Shuckburgh, E. (2000b). Effective diffusion as a diagnostic of atmospheric transport, 2. troposphere and lower stratosphere. *J. Geophys. Res*, **105**, 22795–22810.

Nakamura, N. (1996). Two–dimensional mixing, edge formation and permeability diagnosed in area coordinate. *J. Atmos. Sci.*, **53**(11), 1524–1537.

Nayfeh, A. H. and Mook, D. T. (1979). *Nonlinear Oscillations*. Wiley (New York).

Shuckburgh, E. and Haynes, P. H. (2003). Diagnosing transport and mixing using a tracer-based coordinate system. *Phys. Fluids*, **15**, 3342–3357.

Staniforth, A. N. and Côté, J. (1991). Semi–lagrangian schemes for atmospheric models – A review. *Mon. Wea. Rev.*, **119**, 2206–2223.

Thiffeault, J.-L. (2006). Scalar decay in chaotic mixing. *Transport and Mixing in Geophysical Flows, Lecture Notes in Physics* (Springer, Berlin), **744**, 3–35.

Thiffeault, J.-L., Doering, C. R., and Gibbon, J. D. (2004). A bound on mixing efficiency for the advection-diffusion equation. *J. Fluid Mech.*, **521**, 105–114.

Tirabassi, T. (1989). Analytical air pollution advection and diffusion models. *Water, Air and Soil Pollut.*, **47**, 19–24.

Turner, M. R., Gilbert, A. D., and Thuburn, J. (2008). Effective diffusion of scalar fields in a chaotic flow. *Phys. Fluids*, **20**(10), 107103–1–14.

Wiggins, S. and Ottino, J. M. (2004). Foundations of chaotic mixing. *Philos. Trans. R. Soc. Lond. Ser. A Math. Phys. Eng. Sci.*, **362**(1818), 937–970.

Winters, K. B. and D'Asaro, E. A. (1996). Diascalar flux and the rate of fluid mixing. *J. Fluid Mech.*, **317**, 179–193.